J|A|C|S
ARTICLES
Published on Web 06/02/2007

An Alternating π-Stacked Bisdithiazolyl Radical Conductor

Alicea A. Leitch,[1a] Robert W. Reed,[1a] Craig M. Robertson,[1a] James F. Britten,[1b] Xueyang Yu,[1c] Richard A. Secco,[1c] and Richard T. Oakley*,[1a]

Contribution from the Department of Chemistry, University of Waterloo, Waterloo, Ontario N2L 3G1, Canada, Department of Chemistry, McMaster University, Hamilton, Ontario L8S 4L8, Canada, and Department of Earth Sciences, University of Western Ontario, London, Ontario N6A 5B7, Canada

Received February 20, 2007; E-mail: oakley@uwaterloo.ca

Abstract: A general synthetic route to the resonance-stabilized pyrazine-bridged bisdithiazolyl framework, involving the reductive deprotection of 2,6-diaminopyrazine-bisthiocyanate and cyclization with thionyl chloride, has been developed. An *N*-methyl bisdithiazolyl radical, 4-methyl-4*H*-bis[1,2,3]dithiazolo[4,5-b:5′,4′-e]pyrazin-3-yl, has been prepared and characterized in solution by electron paramagnetic resonance spectroscopy and cyclic voltammetry. Its crystal structure has been determined at several temperatures. At 295 K, the structure belongs to the space group *Cmca* and consists of evenly spaced radicals π-stacked in an alternating ABABAB fashion along the *x*-direction. At 123 K, the space group symmetry is lowered by loss of *C*-centering to *Pccn*, so that the radicals are no longer evenly spaced along the π-stack. At 88 K, a further lowering of space group symmetry to $P2_1/c$ is observed. Extended Hückel Theory band structure calculations indicate a progressive opening of a band gap at the Fermi level in the low-temperature structures. Magnetic susceptibility measurements over the range 4−300 K reveal essentially diamagnetic behavior below 120 K. Variable-temperature single-crystal conductivity (σ) measurements indicate that the conductivity is activated, even at room temperature, with a room-temperature value $\sigma_{RT} = 0.001$ S cm^{-1} and a thermal activation energy $E_{act} = 0.19$ eV. Under an applied pressure of 5 GPa, σ_{RT} is increased by 3 orders of magnitude, but the conductivity remains activated, with E_{act} being lowered to 0.11 eV at 5.5 GPa.

Introduction

Virtually all electrically conductive molecular materials rely on charge transfer (CT) as the means of generating charge carriers.[2] Two components, a donor and an acceptor, are required, although single-component organic metals can be made by incorporating the two moieties into the same molecule.[3] An alternative to the CT paradigm is to construct conductors from molecules that already possess potential charge carriers, that is, to use neutral radicals as the building blocks. As originally proposed,[4] this approach focused on the use of highly delocalized odd-alternant hydrocarbon radicals, notably phenalenyls, derivatives of which have received considerable attention.[5] Spiro-conjugated biphenalenyls, for example, have been shown to display room-temperature conductivities σ_{RT} as high as 10^{-1} S cm^{-1},[6] although a metallic ground state has yet to be demonstrated.

Heteroatom radicals, especially heterocyclic thiazyls, have also been explored as building blocks for molecular conductors.[7,8] Incorporation of nitrogen atoms into spin-bearing sites helps suppress dimerization, and intermolecular interactions between neighboring sulfurs provide a potential pathway for charge migration. However, early attempts to generate super-

(1) (a) University of Waterloo. (b) McMaster University. (c) University of Western Ontario.
(2) For recent reviews on CT conductors, see: (a) Bendikov, M.; Wudl, F.; Perepichka, D. F. *Chem. Rev.* **2004**, *104*, 4891. (b) Jérome, D. *Chem. Rev.* **2004**, *104*, 5565. (c) Geiser, U.; Schlueter, J. A. *Chem. Rev.* **2004**, *104*, 5203. (d) Yamada, J.; Akutsu, H.; Nishikawa, H.; Kikuchi, K. *Chem. Rev.* **2004**, *104*, 5057.
(3) (a) Tanaka, H.; Okano, Y.; Kobayashi, H.; Suzuki, W.; Kobayashi, A. *Science* **2001**, *291*, 285. (b) Kobayashi, A.; Fujiwara, E.; Kobayashi, H. *Chem. Rev.* **2004**, *104*, 5243.
(4) (a) Haddon, R. C. *Nature* **1975**, *256*, 394. (b) Haddon, R. C. *Aust. J. Chem.* **1975**, *28*, 2333. (c) Haddon, R. C. *Aust. J. Chem.* **1975**, *28*, 2343.
(5) (a) Goto, K.; Kubo, T.; Yamamoto, K.; Nakasuji, K.; Sato, K.; Shiomi, D.; Takui, T.; Kubota, M.; Kobayashi, T.; Yakusi, K.; Ouyang, J. *J. Am. Chem. Soc.* **1999**, *121*, 1619. (b) Morita, Y.; Aoki, T.; Fukui, K.; Nakazawa, S.; Tamaki, K.; Suzuki, S.; Fuyuhiro, A.; Yamamoto, K.; Sato, K.; Shiomi, D.; Naito, A.; Takui, T.; Nakasuji, K. *Angew. Chem., Int. Ed.* **2002**, *41*, 1793. (c) Koutentis, P. A.; Chen, Y.; Cao, Y.; Best, T. P.; Itkis, M. E.; Beer, L.; Oakley, R. T.; Brock, C. P.; Haddon, R. C. *J. Am. Chem. Soc.* **2001**, *123*, 3864. (d) Takano, Y.; Taniguchi, T.; Isobe, H.; Kubo, T.; Morita, Y.; Yamamoto, K.; Nakasuji, K.; Takui, T.; Yamaguchi, K. *J. Am. Chem. Soc.* **2002**, *124*, 11122. (e) Small, D.; Zaitsev, V.; Jung, Y.; Rosokha, S. V.; Head-Gordon, M.; Kochi, J. K. *J. Am. Chem. Soc.* **2004**, *126*, 13850. (f) Huang, J.; Kertesz, M. *J. Am. Chem. Soc.* **2003**, *125*, 13334. (g) Huang, J.; Kertesz, M. *J. Am. Chem. Soc.* **2006**, *128*, 1418.
(6) (a) Chi, X.; Itkis, M. E.; Patrick, B. O.; Barclay, T. M.; Reed, R. W.; Oakley, R. T.; Cordes, A. W.; Haddon, R. C. *J. Am. Chem. Soc.* **1999**, *121*, 10395. (b) Itkis, M. E.; Chi, X.; Cordes, A. W.; Haddon, R. C. *Science* **2002**, *296*, 1443. (c) Chi, X.; Itkis, M. E.; Kirschbaum, K.; Pinkerton, A. A.; Oakley, R. T.; Cordes, A. W.; Haddon, R. C. *J. Am. Chem. Soc.* **2001**, *123*, 4041. (d) Chi, X.; Itkis, M. E.; Reed, R. W.; Oakley, R. T.; Cordes, A. W.; Haddon, R. C. *J. Phys. Chem. B* **2002**, *106*, 8278. (e) Mandal, S. K.; Itkis, M. E.; Chi, X.; Samanta, S.; Lidsky, D.; Reed, R. W.; Oakley, R. T.; Tham, F. S.; Haddon, R. C. *J. Am. Chem. Soc.* **2005**, *127*, 8185. (f) Pal, S. K.; Itkis, M. E.; Tham, F. S.; Reed, R. W.; Oakley, R. T.; Haddon, R. C. *Science* **2005**, *309*, 281. (g) Mandal, S. K.; Samanta, S.; Itkis, M. E.; Jensen, D. W.; Reed, R. W.; Oakley, R. T.; Tham, F. S.; Donnadieu, B.; Haddon, R. C. *J. Am. Chem. Soc.* **2006**, *128*, 1982.
(7) (a) Rawson, J. M.; Alberola, A.; Whalley, A. *J. Mater. Chem.* **2006**, *16*, 2560. (b) Hicks, R. G. *Org. Biomol. Chem.* **2007**, *5*, 1321.
(8) (a) Cordes, A. W.; Haddon, R. C.; Oakley, R. T. *Adv. Mater.* **1994**, *6*, 798. (b) Cordes, A. W.; Haddon, R. C.; Oakley, R. T. In *The Chemistry of Inorganic Ring Systems*; Steudel, R., Ed.; Elsevier: Amsterdam, 1992; p 295. (c) Beer, L.; Cordes, A. W.; Myles, D. J. T.; Oakley, R. T.; Taylor, N. J. *CrystEngChem* **2000**, *2*, 109.

Chart 1

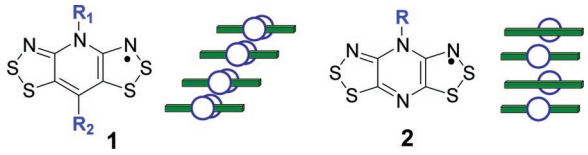

1 **2**

imposed radical π-stacks invariably afforded S−S linked π-dimer stacks, that is, charge density wave (CDW) or Peierls[9] distorted structures which were insulating or weakly semiconducting.[8] A potentially more serious problem with early thiazyl radical materials was their high onsite Coulomb repulsion energy U.[10] Thus, even when radical dimerization could be avoided, intermolecular orbital overlap and the associated solid-state bandwidth W were insufficient to overcome Coulomb repulsion, and the materials were trapped in Mott insulating states.[11] Attempts to improve conductivity have therefore focused on the development of more delocalized (low U) radicals which display a strong network of intermolecular interactions in the solid state, and hence a large bandwidth W, the criterion for a metallic ground state being that $W > U$.

With these energetic and bandwidth criteria in mind, we prepared a variety of resonance-stabilized radicals,[12] including those based on the bisdithiazolyl framework **1** (Chart 1).[13] A notable feature of these materials is that they do not form π-dimers in the solid state, in part because of the buffering effect of the beltline R_1 and R_2 substituents, but also because of the extent of spin delocalization in the radicals.[14−16] However, while the estimated gas-phase disproportionation enthalpies ΔH_{disp} found for these materials suggest a reduced value for U in the solid state,[17] their bulk conductivities remain activated, with thermal activation energies $E_{act} = 0.4-0.5$ eV and room-temperature conductivities $\sigma_{RT} \approx 10^{-6}$ S cm^{-1}. Extended Hückel Theory (EHT) band structure calculations have indicated bandwidths W of less than 0.5 eV, values which are comparable to those found in many conductive CT salts, but clearly still too small to offset U, which is a maximum for a half-filled band, that is, an $f = {}^1/_2$ system. This conclusion prompts the question as to how to modify the bisdithiazolyl framework **1** in order to increase the solid-state bandwidth W sufficiently to overcome the onsite Coulomb repulsion U.

Chart 2

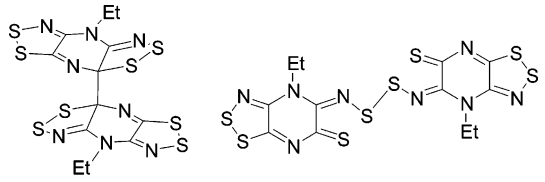

α–[**2**]$_2$ (R = Et) β–[**2**]$_2$ (R = Et)

We are approaching this design challenge in two ways. The first involves the replacement of sulfur by selenium, a tactic employed early on in the design of CT salts,[18] and initial results are encouraging.[19] The second approach, the one addressed herein, involves the replacement of the central pyridine ring of **1** by a pyrazine bridge, as in **2**. While the values of U for both **1** and **2** are expected to be comparable, the more exposed periphery of **2**, with its less heavily substituted framework, should allow for stronger intermolecular interactions, and hence an improved bandwidth W. We also hoped to be able to move away from the slipped π-stack arrays found for **1** to alternating but vertically aligned ABABAB π-stacks (Chart 1), an adjustment expected to afford greater overlap and hence larger bandwidth.[15]

We recently reported the first example of **2**, with R = Et. To our surprise, this compound crystallized as closed-shell dimers instead of π-stacked radicals. Moreover, two very different modes of association were observed (Chart 2), one involving a localized C−C σ-bond (α-[**2**]$_2$, R = Et) and the other a lateral S−S σ-bond (β-[**2**]$_2$, R = Et).[20] We have now prepared and structurally characterized the corresponding methyl derivative **2** (R = Me). In contrast to the ethyl derivative, this compound adopts a crystal structure in which the molecules are π-stacked in alternating ABABAB arrays, as shown in Chart 1. This arrangement affords a material with a room-temperature conductivity that is markedly improved over those seen for all derivatives of **1**; indeed, the value of $\sigma_{RT} \approx 10^{-3}$ S cm^{-1} is the highest ever observed for a thiazyl radical conductor. The material is not, however, a metal. Low-temperature crystallographic studies reveal a series of changes in space group associated with the opening of a band gap at the Fermi level and the formation of a semiconducting ground state. In this paper, we describe the preparation and structural characterization of **2** (R = Me). Variable-temperature magnetic susceptibility and conductivity measurements, the latter at ambient and elevated (<5.5 GPa) pressures, are also presented, and the results are interpreted in the light of the EHT band structure calculations.

Results and Discussion

Synthesis. Construction of the pyrazine-bridged bisdithiazolyl framework **2** required a lengthy synthetic sequence (Scheme

(9) Peierls, R. C. *Quantum Theory of Solids*; Oxford University Press: London, 1955; p 108.

(10) (a) Barclay, T. M.; Cordes, A. W.; George, N. A.; Haddon, R. C.; Itkis, M. E.; Mashuta, M. S.; Oakley, R. T.; Patenaude, G. W.; Reed, R. W.; Richardson, J. F.; Zhang, H. *J. Am. Chem. Soc.* **1998**, *120*, 352. (b) Boeré, R. T.; Roemmele, T. L. *Coord. Chem. Rev.* **2000**, *210*, 369. (c) Kaszynski, P. *J. Phys. Chem. A* **2001**, *105*, 7626. (d) Kaszynski, P. *J. Phys. Chem. A* **2001**, *105*, 7615.

(11) Mott, N. F. *Metal−Insulator Transitions*; Taylor and Francis: London, 1990.

(12) Beer, L.; Haddon, R. C.; Itkis, M. E.; Leitch, A. A.; Oakley, R. T.; Reed, R. W.; Richardson, J. F.; VanderVeer, D. G. *Chem. Commun.* **2005**, 1218.

(13) Cordes, A. W.; Haddon, R. C.; Oakley, R. T. *Phosphorus, Sulfur, Silicon Relat. Elem.* **2004**, *179*, 673.

(14) Beer, L.; Brusso, J. L.; Cordes, A. W.; Haddon, R. C.; Itkis, M. E.; Kirschbaum, K.; MacGregor, D. S.; Oakley, R. T.; Pinkerton, A. A.; Reed, R. W. *J. Am. Chem. Soc.* **2002**, *124*, 9498.

(15) (a) Beer, L.; Brusso, J. L.; Cordes, A. W.; Haddon, R. C.; Godde, E.; Itkis, M. E.; Oakley, R. T.; Reed, R. W. *Chem. Commun.* **2002**, 2562. (b) Beer, L.; Britten, J. F.; Brusso, J. L.; Cordes, A. W.; Haddon, R. C.; Itkis, M. E.; MacGregor, D. S.; Oakley, R. T.; Reed, R. W.; Robertson, C. M. *J. Am. Chem. Soc*. **2003**, *125*, 14394.

(16) Beer, L.; Britten, J. F.; Clements, O. P.; Haddon, R. C.; Itkis, M. E.; Matkovich, K. M.; Oakley, R. T.; Reed, R. W. *Chem. Mater*. **2004**, *16*, 1564.

(17) ΔH_{disp} is the enthalpy change for the conversion of two gas-phase radicals R into a cation/anion pair, i.e., 2 R ⇄ $R^+ + R^-$, and is equal to the difference between the ionization potential (IP) and electron affinity (EA). The cell potential, $E_{cell} = E_{1/2}(ox) - E_{1/2}(red)$, is the difference between the half-wave potentials for the oxidation and reduction processes.

(18) (a) Beechgaard, K.; Cowan, D. O.; Bloch, A. N. *J. Chem. Soc., Chem. Commun*. **1974**, 937. (b) Engler, E. M.; Patel, V. V. *J. Am. Chem. Soc*. **1974**, *96*, 7376.

(19) (a) Beer, L.; Brusso, J. L.; Haddon, R. C.; Itkis, M. E.; Leitch, A. A.; Oakley, R. T.; Reed, R. W.; Richardson, J. F. *Chem. Commun*. **2005**, 1543. (b) Beer, L.; Brusso, J. L.; Haddon, R. C.; Itkis, M. E.; Kleinke, H.; Leitch, A. A.; Oakley, R. T.; Reed, R. W.; Richardson, J. F.; Secco, R. A.; Yu, X. *J. Am. Chem. Soc.* **2005**, *127*, 1815. (c) Brusso, J. L.; Cvrkalj, K.; Leitch, A. A.; Oakley, R. T.; Reed, R. W.; Robertson, C. M. *J. Am. Chem. Soc.* **2006**, *128*, 15080. (d) Brusso, J. L.; Derakhshan, S.; Itkis, M. E.; Kleinke, H.; Haddon, R. C.; Oakley, R. T.; Reed, R. W.; Richardson, J. F.; Robertson, C. M.; Thompson, L. K. *Inorg. Chem*. **2006**, *45*, 10958.

(20) Leitch, A. A.; McKenzie, C. E.; Oakley, R. T.; Reed, R. W.; Richardson J. F.; Sawyer, L. D. *Chem. Commun*. **2006**, 1088.

Scheme 1

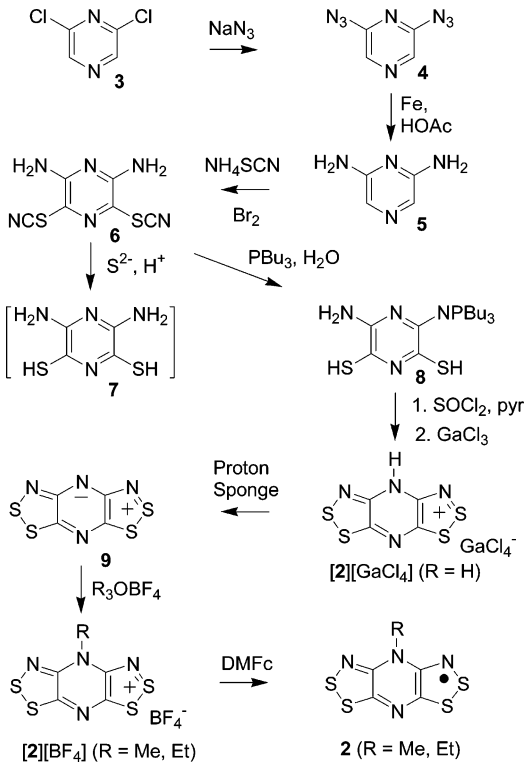

1), the first step of which was the preparation of 2,6-diaminopyrazine **5**. This latter compound can be generated in small quantities by the hydrogenation of the corresponding diazide **4**, which is itself readily prepared from dichloropyrazine **3**.[21] With more convenient reagents, for example, sodium borohydride, only one azide is fully reduced, while the other is trapped as a tetrazole.[21] We have found, however, that complete reduction of both azides can be achieved using iron in aqueous acetic acid;[22] after an alkaline workup, the diamino compound **5** can be extracted in 70% yield (from **3**). In previous studies, we showed that the pyridine-bridged bisdithiazolyl framework **1** can be made, in a single step, via a double Herz cyclization of diaminopyridine with sulfur monochloride.[14−16] Unfortunately, the 3,5-positions of diaminopyrazine are less susceptible to electrophilic substitution than are the corresponding sites in diaminopyridine, as a result of which double Herz cyclization of **5** with sulfur monochloride fails. Assembly of the desired tricyclic skeleton of **2** therefore required, as a first step, the conversion of the diaminopyrazine **5** to its bisthiocyanate derivative **6**. Reductive deprotection of thiocyanates has typically been achieved with aqueous sodium sulfide, followed by acidification to afford the diamino-dithiol **7**.[4,23] However, the use of this approach on **6** afforded, after an acidic workup, an intractable brown solid that did not undergo a cyclization reaction with thionyl chloride or sulfur monochloride.

We therefore turned to the use of tributylphosphine, a reagent commonly employed in the reductive deprotection of thiocyanates.[24] Accordingly, the reaction of **6** with Bu_3P in anhydrous MeCN afforded a deep orange solution, and addition of small amounts of water to this mixture led to the precipitation of the monosubstituted aminophosphiniminodithiol **8** as an orange microcrystalline solid; this material served as an effective alternative to **7**.[25] Reaction of **8** with thionyl chloride in the presence of pyridine afforded the desired bisdithiazolylium framework in the form of the protonated salt [**2**][Cl] (R = H). The crude insoluble chloride was purified by conversion to a tetrachlorogallate, which could be deprotonated with Proton-Sponge to afford the ternary zwitterion **9**. Alkylation of this free base with Meerwein salts R_3OBF_4 (R = Me, Et) caused some initial difficulties, as the product was invariably contaminated by protonated material. However, when the alkylation was performed in the presence of Proton-Sponge, protonation was effectively suppressed, and the desired N-alkylated salts [**2**][BF_4] (R = Me, Et) were obtained in good yield.

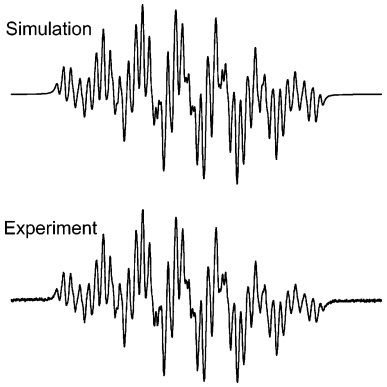

Figure 1. EPR spectrum of **2** (R = Me) in CH_2Cl_2, SW = 3 mT; for the simulation, L/G = 0.01 mT and LW = 0.024 mT.

Chemical reduction of [**2**][BF_4] (R = Me, Et) was achieved using decamethylferrocene (DMFc) in MeCN. In the case of R = Et, the reaction afforded a light brown crystalline solid which was sublimed in vacuo to yield a mixture of amber blocks of α-[**2**]$_2$ (R = Et) and black needles of β-[**2**]$_2$ (R = Et). The structures, relative energetics, and thermal interconversion of these two dimers were described earlier.[20] The methyl compound **2** (R = Me) crystallizes directly from the reaction mixture as copper-colored needles; its crystal structure and transport properties are described below.

Electron Paramagnetic Resonance Spectroscopy and Cyclic Voltammetry. The extent of spin delocalization in the pyrazine-bridged radicals **2** (R = Me, Et) has been probed by electron paramagnetic resonance (EPR) spectroscopy and cyclic voltammetry. The X-band EPR spectrum of **2** (R = Me), recorded on a sample dissolved in CH_2Cl_2 at room temperature, is shown in Figure 1, along with a simulation from which the ^{14}N and ^{1}H hyperfine coupling constants were extracted. The coupling constants a_N and a_H for both radicals **2** (R = Me, Et) are listed in Table 1; for purposes of comparison, those of the related pyridine-bridged radicals **1** (R_1 = Me, Et; R_2 = H) are also provided. In both pairs of radicals, the hyperfine patterns

(21) Shaw, J. T.; Brotherton, C. E.; Moon, R. W.; Winland, M. D.; Anderson, M. D.; Kyler, K. S. *J. Heterocycl. Chem.* **1980**, *11*, 17.
(22) Zienkiewicz, J.; Kaszynski, P.; Young, V. G., Jr. *J. Org. Chem.* **2004**, *69*, 2551.
(23) (a) Baker, A. J.; Hill, S. A. *J. Chem. Soc.* **1962**, 3464. (b) Lochon, P.; Méheux, P.; Néel, J. *Bull. Soc. Chim. Fr.* **1967**, *11*, 4387. (c) Okada, M.; Marvel, C. S. *J. Polym. Sci., Part A-1* **1968**, *6*, 1259.
(24) Flowers, W. T.; Holt, G.; Omogbal, F.; Poulos, C. P. *J. Chem. Soc., Perkin Trans. 1* **1976**, 2394.
(25) The structural constitution of this compound has been confirmed by single-crystal X-ray diffraction. The crystals belong to the trigonal space group $P3_12_1$, with $a = b = 12.0557(4)$ Å, $c = 55.325(4)$ Å, $Z = 12$ (at $T = 200$ K). There are two hydrogen-bonded molecules in the asymmetric unit, each with the molecular formula shown in Scheme 1.

Table 1. Hyperfine Coupling Constants (mT), *g*-Values, and Half-Wave Potentials[a]

	1 (R_1 = Me, R_2 = H)	**1** (R_1 = Et, R_2 = H)	**2** (R = Me)	**2** (R = Et)
a_N	0.313 (2N) 0.062 (1N)	0.318 (2N) 0.061 (1N)	0.309 (2N) 0.073 (1N) 0.266 (1N)	0.313 (2N) 0.073 (1N) 0.266 (1N)
a_H (CH)	0.230 (1H)	0.228 (1H)		
a_H (NR)	0.034 (NCH_3)	<0.02 (NCH_2CH_3)	0.053 (NCH_3)	0.025 (NCH_2CH_3)
g-value	2.0082	2.0082	2.0087	2.0087
$E_{1/2}^{-1/0}$	−0.95[c]	−0.95[c]	−0.870[c]	−0.853[c]
$E_{1/2}^{0/+1}$	−0.130	−0.146	−0.0104	−0.0291
$E_{1/2}^{+1/+2}$	1.294	1.272	1.610	1.585
E_{cell}[b]	0.77[d]	0.76[d]	0.82[d]	0.85[d]

[a] $E_{1/2}$-values (volts) in MeCN, referenced to saturated calomel electrode (SCE). [b] $E_{cell} = E_{1/2}(0/+1) - E_{1/2}(-1/0)$. [c] Irreversible behavior; E_{pc}-value quoted. [d] E_{cell} estimated as $E_{pc}(0/+1) - E_{pc}(-1/0)$.

are dominated by coupling to two equivalent dithiazolyl nitrogens, the value of a_N being approximately one-half of that observed in monofunctional 1,2,3-dithiazolyl radicals.[26] There is also a weaker coupling to the pyrazine nitrogen and to the N-methyl (or N-ethyl) protons, as well as a relatively large hyperfine interaction with the basal nitrogen of the pyrazine ring. In the pyridine-bridged systems, this is replaced by coupling to the basal CH proton.

The results of cyclic voltammetric measurements on the [**2**]-[BF_4] salts (R = Me, Et), presented in the form of half-wave potentials $E_{1/2}$, are summarized in Table 1. Both radicals show a reversible 0/+1 wave in the range −0.01 to −0.03 V vs SCE, individual values being shifted anodically by some 120 mV with respect to the analogous couples of **1** (R_1 = Me, Et; R_2 = H), as expected from the more electronegative pyrazine core. A more anodic reversible +1/+2 wave is also present. As in **1** (R_1 = Me, Et; R_2 = H), reduction of the radical to the anion (the −1/0 couple) is irreversible, a feature which we have previously attributed to the cleavage of one of the S−S[27] (or S−N)[28] bonds upon reduction of the radical. The cell potential values E_{cell} cited in Table 1 are thus only estimates based on the difference between the cathodic peak potentials (E_{pc}) of the oxidation and reduction processes. Nonetheless, the trends in both $E_{1/2}$ and E_{cell} map well onto those observed for the pyridine-based radicals **1**, and are broadly consistent with the computed gas-phase IP, EA, and disproportionation enthalpy ΔH_{disp} data previously estimated for resonance-stabilized bisdithiazolyls.[14,15]

Crystal Structure. Copper-colored needles of **2** (R = Me) suitable for X-ray and single-crystal conductivity measurements were grown by slow, diffusion-controlled mixing of solutions of [**2**][BF_4] and DMFc. In order to interpret and understand the transport properties (vide infra) of the material, its crystal structure was determined at 295, 123, and 88 K. Crystal data at these temperatures are provided in Table 2, and pertinent intermolecular S−S′ and S−N′ contacts are listed in Table 3. Figure 2 shows ORTEP drawings of the asymmetric units at the three temperatures.

At 295 K, the crystal structure of **2** (R = Me) belongs to the orthorhombic space group *Cmca* and is based on arrays of *evenly spaced* radicals π-stacked along the *x*-direction. Within the molecular units, bond distances and angles are typical of a bisdithiazolyl radical.[14,15] Two views of the crystal structure, showing the unit cell packing and the lateral S−S′ and S−N′ interactions (Table 3) between neighboring molecules, are provided in Figure 3. There are eight radicals in the unit cell, all of which lie on crystallographic mirror planes at $x = 0$ and

Table 2. Crystallographic Data for **2** (R = Me)

	T		
	88(2) K	123(2) K	295(2) K
formula	$C_5H_3N_4S_4$	$C_5H_3N_4S_4$	$C_5H_3N_4S_4$
fw	247.35	247.35	247.35
a, Å	9.244(2)	6.5456(6)	6.6488(2)
b, Å	6.5344(17)	9.2558(8)	27.2177(5)
c, Å	27.035(7)	27.040(2)	9.2797(2)
β, deg	90.004(4)	−	−
V, Å^3	1633.0(7)	1638.2(2)	1679.30(7)
ρ(calcd), g cm^{-3}	2.012	2.006	1.957
space group	$P2_1/c$	*Pccn*	*Cmca*
Z	8	8	8
μ, mm^{-1}	1.11	10.266	10.015
λ, Å	0.71073	1.54178	1.54178
data/restraints/ parameters	4040/182/ 236	1399/0/ 130	829/0/ 79
solution method	direct methods	direct methods	direct methods
R, R_w (on F^2)[a]	0.0720, 0.1398	0.0570, 0.1617	0.0387, 0.1105

[a] $R = [\sum||F_o| - |F_c||]/[\sum|F_o|]$ for $I > 2\sigma(I)$; $R_w = \{[\sum w||F_o|^2 - |F_c|^2|^2]/[\sum(w|F_o|^4)]\}^{1/2}$.

Table 3. Summary of Contacts and Angles in **2** (R = Me)

Contacts[a]	88 K *$P2_1/c$*	123 K *Pccn*	295 K *Cmca*
	Lateral (σ)		
S1−S2′	3.270(7), 3.294(7)	3.281(2)	3.305(1)
S2−S4′	3.418(8), 3.449(7)	3.435(2)	3.466(1)
S1−N4′	3.179(14), 3.155(13)	3.166(5)	3.192(3)
S2−N4′	3.099(12), 3.193(11)	3.152(5)	3.179(3)
S3−N3′	3.023(13), 2.939(14)	2.989(4)	3.059(3)
	Intrastack (π)		
S1−S4′	3.727(6), 3.928(6)	3.760(2)	3.865(1)
S4−S1′	3.750(6), 3.841(6)	3.874(2)	3.865(1)
S2−S2′	3.627(4), 4.001(4)	3.662(3), 3.966(3)	3.851(1)
	Interstack (π)		
S1−S2′	3.667(7), 3.844(6)	3.697(2)	3.831(1)
S2−S1′	3.828(7), 3.684(6)	3.831(2)	3.831(1)
S3−S3′	4.120(3), 3.948(3)	3.964(3), 4.121(3)	4.093(1)
S4−S4′	4.079(4), 3.690(4)	3.723(3), 4.056(3)	3.936(1)
δ[b]	0.026(8), 0.024(8)	0.018(3)	0
φ[c]	2.6(3), 2.8(3)	2.17(10)	0

[a] Distances in angstroms. [b] Maximum deviation from the mean molecular plane. [c] Tilt angle of the perpendicular to mean plane from the stacking axis.

(26) (a) Cordes, A. W.; Mingie, J. R.; Oakley, R. T.; Reed, R. W.; Zhang, H. *Can. J. Chem.* **2001**, *79*, 1352. (b) Barclay, T. M.; Beer, L.; Cordes, A. W.; Oakley, R. T.; Preuss, K. E.; Taylor, N. J.; Reed, R. W. *Chem. Commun.* **1999**, 531. (c) Preston, K. F.; Sutcliffe, L. H. *Magn. Reson. Chem.* **1990**, *28*, 189.
(27) Antonello, S.; Benassi, R.; Gavioli, G.; Taddei, F.; Maran, F. *J. Am. Chem. Soc.* **2002**, *124*, 7529.
(28) Alternatively, N−S bond cleavage could occur. See, for example: Barclay, T. M.; Cordes, A. W.; Goddard, J. D.; Mawhinney, R. C.; Oakley, R. T.; Preuss, K. E.; Reed, R. W. *J. Am. Chem. Soc.* **1997**, *119*, 12136.

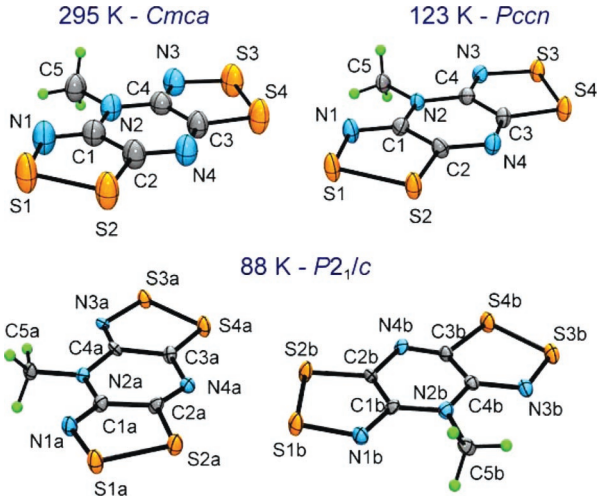

Figure 2. ORTEP drawings of the asymmetric units of **2** (R = Me) at 295, 123, and 88 K, showing atom numbering schemes.

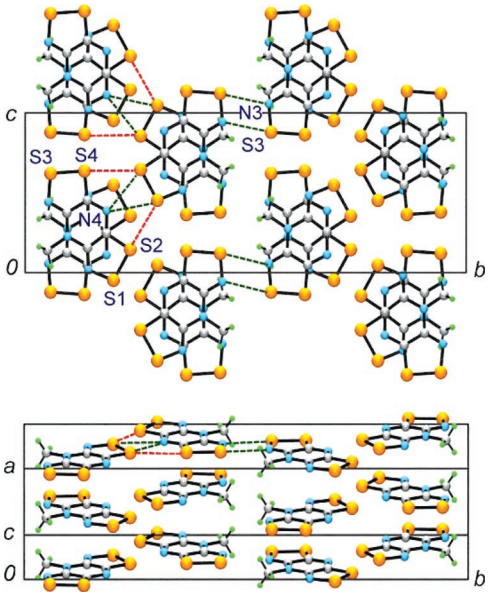

Figure 3. Two views of the *Cmca* unit cell of **2** (R = Me) at 295 K. Lateral intermolecular S−S′ contacts (in red) and S−N′ contacts (in green) are defined in Table 3.

$^1/_2$, with consecutive plates along the *x*-direction related by the *a*-glide at $z = {}^1/_4$ and $^3/_4$ so as to produce superimposed ABABAB arrays with an interplanar separation of *a*/2, or 3.347-(2) Å. This arrangement (Figure 4) affords a series of intracolumnar S−S′ contacts (Table 3) up and down the π-stack which, although outside of the normal van der Waals range,[29] are well oriented for strong π-overlap. The *c*-glide operation at $y = {}^1/_4$ and $^3/_4$ generates pairs of dovetailed arrays of these stacks, the two halves of which are laced together by a network (Figure 4 and Table 3) of ladder-like intercolumnar π-type S−S′ contacts (S1−S2′, S3−S3′, and S4−S4′) that extend lattice-wide along both the *x*- and *z*-directions. The packing of the radicals into double rows of interconnected π-stacks running parallel to the *z*-direction gives rise to the dovetailed motif shown in Figure 5. These double rows are then locked together by the four-center σ-type centrosymmetric S3−N3′ interactions noted earlier (Figure 3). As a result of the absence of intermolecular S−S′ contacts, electronic communication in the *y*-direction is minimal.

(29) Bondi, A. J. *Phys. Chem.* **1964**, *68*, 441.

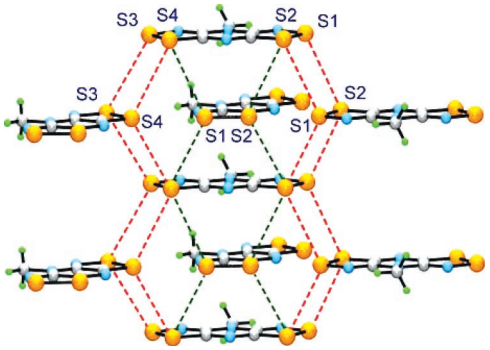

Figure 4. Alternating ABABAB π-stacks of **2** (R = Me) at 295 K. Intrastack S−S′ contacts (in green) and interstack S−S′ contacts (in red) are defined in Table 3.

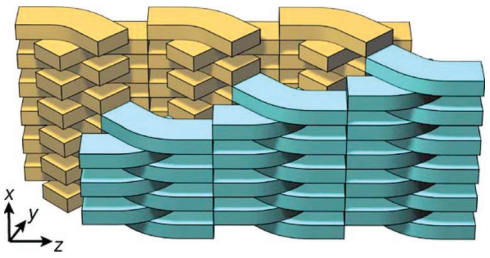

Figure 5. Cross-linking of rows of π-stacks in **2** (R = Me) in the *Cmca* space group at 295 K.

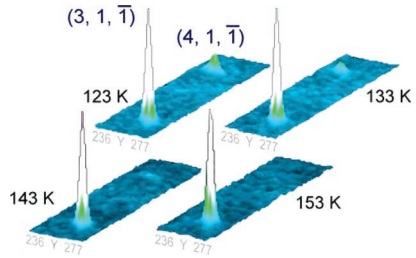

Figure 6. Appearance of the (4,1,1̄) reflection below 143 K, heralding the loss of *C*-centering. The strong (3,1,1̄) reflection is allowed in both *P*- and *C*-lattices.

Cooling crystals of **2** (R = Me) leads to small but expected contractions in unit cell dimensions and intramolecular bond lengths. A second data set, collected at 123 K, could be solved and refined in the original space group (*Cmca*), but the asymmetry of the thermal ellipsoids (elongation along the stacking direction) apparent in the 295 K structure (Figure 2) was more serious and obliged us to consider a symmetry-lowering distortion. A full search over all observed reflections at 123 K revealed several violations of *C*-centering and a change in Bravais lattice from *C* to *P*. In order to establish the temperature range for this transition, we monitored the evolution of the (4, 1, 1̄) reflection as a function of temperature (Figure 6). At 153 K, this peak was absent, as expected ((*h*+*k*) odd) for a *C*-lattice. However, near 143 K, the reflection emerged from the background, thereby signaling the transition to a *P*-lattice. Further cooling to 123 K led to an increase in intensity of this peak. Subsequent evaluation of the systematic absences of the 123 K data in a primitive orthorhombic setting allowed us to conclude that the correct space group is *Pccn*, and the structure reported here is based on that assignment.

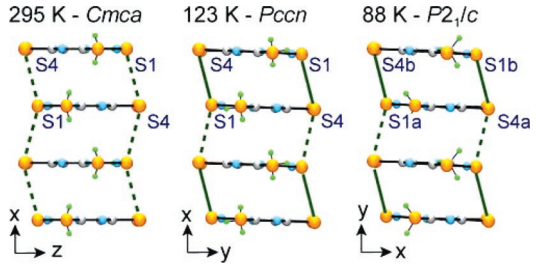

Figure 7. Transformation of evenly spaced radical π-stacks to π-dimer stacks as a function of temperature. Intermolecular S1−S4′ contacts (Table 3) are shown in green.

Concomitant with loss of *C*-centering is a crossover in the definition of the *b*- and *c*-axes, as may be seen in Table 2. More importantly, the molecular plates along the ABABAB π-stacks are free to move away from their otherwise fixed positions at $x = 0$ and $^1/_2$. The resulting deviations (Table 3) are, however, small. The molecules remain essentially planar ($\delta = 0.018$ Å) and tilt very slightly ($\phi = 2.2°$) away from perpendicularity with respect to the stacking direction (Figure 7). The network of intermolecular interactions also changes.[30] Consecutive molecules along the π-stack in the new unit cell are related by symmetry (a 2-fold rotation about *c*) but are not equally spaced up and down the π-stacks. As a result, the four previously equivalent S1−S4′ contacts associated with a given molecule separate into two pairs, at 3.760(2) and 3. 874(2) Å, above and below the molecule, respectively, to produce a small but significant alternation in the plate-to-plate separation. The four ladder-like S1−S2′ contacts which were identical in *Cmca* evolve into equivalent pairs above and below the molecule. Finally, the S3−S3′ and S4−S4′ interactions separate into four distinct contacts (two long and two short).

A third data set was collected at 88 K, and inspection of the systematic absences indicated a loss of two of the three glide planes of *Pccn* and a further reduction in space group symmetry to primitive monoclinic. The presence of the remaining glide plane established the setting to be $P2_1/c$, and the structure was solved and refined in this space group.[31] The slight increase in the *R*-value (Table 2) can be ascribed to the need to refine a greater number of weak reflections and a merohedral twinning arising from the pseudo-orthorhombic nature of the lattice. There is a switchover in unit cell vectors ($a \leftrightarrow b$) from the *Pccn* settings (Table 2), but the cell constants remain close to those seen at 123 K. The symmetry lowering leads to two crystallographically independent molecules per asymmetric unit, so that consecutive molecules along the ABABAB π-stacks are no longer equivalent. The two molecules are nonetheless closely related, being nearly planar ($\delta = 0.026$ and 0.24 Å), and the tilt angle ϕ for both increases only slightly (to 2.6° and 2.8°) relative to that seen at 123 K. The four possible S1−S4′ contacts (Table 3 and Figure 7) are now completely independent but fall into two groups (long and short), as seen at 123 K, indicative of a slight but continued migration toward a bond-alternating π-dimer stack.

(30) Detailed illustrations of these changes are provided in the Supporting Information.

(31) The 88 K data set could be solved in *Pccn*, if over 40 systematic absence violations were ignored, but attempts to refine the solution gave rise to unreasonably large thermal ellipsoids and a high *R*-factor. Lower symmetry orthorhombic space groups were considered, but none was satisfactory. Only when the space group symmetry was lowered to monoclinic $P2_1/c$ were all systematic absence requirements met and a satisfactory refinement achieved. This change allowed atoms to move away from positions otherwise defined by the extra glide planes of *Pccn*.

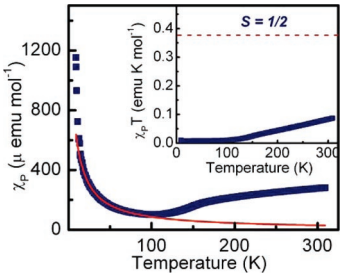

Figure 8. Plots of χ_P and $\chi_P T$ (inset) versus T for **2** (R = Me).

Magnetic Susceptibility Measurements. Magnetic susceptibility measurements on **2** (R = Me), recorded on a Faraday balance over the temperature range 9−300 K, are shown in Figure 8. The results are presented in the form of a plot of χ_P, the paramagnetic susceptibility after correction for diamagnetic contributions ($\chi_D = 117.29 \times 10^{-6}$ emu mol^{-1}).[32] At ambient temperature, the material is weakly paramagnetic, with $\chi_P = 277 \times 10^{-6}$ emu mol^{-1} at 300 K. With decreasing temperatures, the value of χ_P decreases slightly, reaching a minimum value of 101×10^{-6} emu mol^{-1} near 100 K. Further cooling leads to a rapid increase in χ_P, which we interpret as heralding the presence of paramagnetic defects in the lattice. Such features are commonly observed in crystalline radicals, and their susceptibility should follow Curie-Weiss behavior. Consistently, a Curie-Weiss fit (shown in Figure 8) to the data between $T =$ 12 and 81 K provides values of $C = 0.0091$ emu K mol^{-1} and $\Theta = -5.2$ K. Also illustrated in Figure 8 is a plot of $\chi_P T$ versus temperature. Below 100 K, $\chi_P T$ remains approximately constant, with a value of 2% of that expected (0.375) for a Curie paramagnet with $S = ^1/_2$. This residual paramagnetism amounts to the contribution of the defect electrons to the total moment. Above 120 K, the value of $\chi_P T$ begins to increase steadily from its threshold value, reaching a value of 0.09 emu K mol^{-1} at 300 K; this corresponds to a spin defect concentration of approximately 25%. Similar paramagnetic enhancements of otherwise diamagnetic π-dimer stacks have been observed elsewhere,[33,34] and these have been attributed to the uncoupling of the weak intradimer bonds and the generation of additional spin defects.

Conductivity Measurements. We have carried out four-probe conductivity (σ) measurements on both pressed pellet and single-crystal samples of **2** (R = Me). The results are self-consistent: the conductivity at 295 K from a pressed pellet sample is 6.4×10^{-4} S cm^{-1}, while for a single crystal σ (295 K) increases to 9.7×10^{-4} S cm^{-1}. These values constitute the highest conductivities ever observed for a thiazyl radical. The temperature dependence of the single-crystal conductivity over the range 73−295 K, shown in Figure 9, confirms that the conductivity is activated. It is also apparent that the thermal activation energy E_{act} is itself temperature dependent, with two distinct and approximately linear log σ vs $1/T$ regimes, one spanning the range 295−120 K, the other 120−80 K. In the high-temperature range, the derived E_{act} is 0.19 eV, while in

(32) Estimated from Pascal's constants. Carlin, R. L. *Magnetochemistry*; Springer-Verlag: New York 1986.

(33) (a) Beekman, R. A.; Boeré, R. T.; Moock, K. H.; Parvez, M. *Can. J. Chem.* **1998**, *76*, 85. (b) Andrews, M. P.; et al. *J. Am. Chem. Soc.* **1991**, *113*, 3559. (c) Cordes, A. W.; Haddon, R. C.; Hicks, R. G.; Kennepohl, D. K.; Oakley, R. T.; Palstra, T. T. M.; Schneemeyer, L. F.; Scott, S. R.; Waszczak, J. V. *Chem. Mater.* **1993**, *5*, 820.

(34) Barclay, T. M.; Cordes, A. W.; Haddon, R. C.; Itkis, M. E.; Oakley, R. T.; Reed, R. W.; Zhang, H. *J. Am. Chem. Soc.* **1999**, *121*, 969.

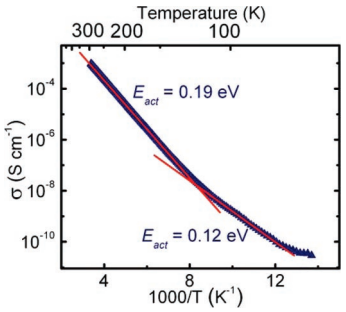

Figure 9. Single-crystal conductivity of **2** (R = Me) at ambient pressure, with derived E_{act}-values.

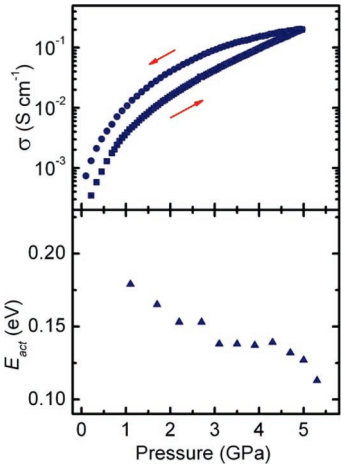

Figure 10. Pressure dependence of σ (294 K) (top) and E_{act} (bottom) of **2** (R = Me).

the low-temperature region it is 0.12 eV. Below 80 K, the activation energy appears to drop even further, but there are insufficient data to warrant a numerical analysis. An interpretation of these changes is provided below.

We have also probed the pressure dependence of the conductivity of **2** (R = Me) using a cubic anvil press. As illustrated in Figure 10, the conductivity σ (at 294 K) increases steadily with applied pressure, reaching a value near 0.2 S cm^{-1} at 5.0 GPa. Analysis of the temperature dependence (from 20 to 90 °C) of the conductivity indicates that it remains activated over the entire pressure range studied. From a series of plots of log σ vs $1/T$, we have derived the activation energies E_{act} as a function of pressure, and these results are also plotted in Figure 10. Initially the value of E_{act} decreases steadily to a plateau value near 0.13 eV between 3 and 4 GPa. It then begins to decrease more rapidly around 5 GPa, reaching a value of 0.11 eV at 5.5 GPa, the limiting pressure of the apparatus. Comparison of these results with those obtained from the slipped π-stack bisdithiazolyl **1** (R_1 = Me, R_2 = Ph)[35] reveals that the pressure responses of the conductivity for the two compounds are similar; that is, both show an increase in conductivity of about 3 orders of magnitude over a 5 GPa range. However, for the present compound the decrease in the activation energy with increasing pressure is somewhat smaller.

Near-Infrared Spectrum. As a complement to the conductivity measurements, and the activation energies derived therefrom, we have examined the near-infrared spectrum of a single-crystal sample of **2** (R = Me) at ambient temperature. Figure 11 shows the IR transmittance over the range 650−11000 cm^{-1}. In the mid-IR region, between 650 and 3100 cm^{-1}, there is a series of absorptions arising from molecular vibrations of the molecule. Underlying these modes, however, is a strong background absorption which, we believe, arises from solid-state processes (vide infra). In addition, there is a strong, well-developed, low-lying absorption cutoff beyond 3000 cm^{-1} which, as will be described below, corresponds to the valence-to-conduction band excitation of a semiconductor. The optical energy gap E_g has a threshold value near 0.48 eV, increasing to near 0.75 eV at the transmission cutoff.

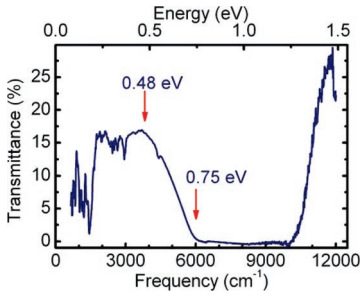

Figure 11. Single-crystal IR transmission spectrum of **2** (R = Me).

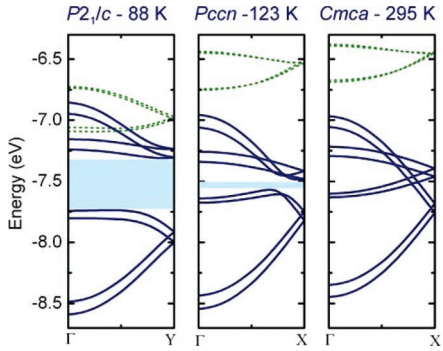

Figure 12. EHT dispersion curves for the three crystal structures of **2** (R = Me), showing the emergence of a band gap at lower temperatures. The solid blue lines are the COs arising from the radical SOMOs. Higher-lying orbitals (green dashed lines) overlap in the $P2/_1c$ structure.

Band Structures. In order to develop an understanding of the electronic structure of **2** (R = Me), and to rationalize the results of the crystallographic, magnetic, conductivity, and optical measurements, we have carried out EHT band structure calculations on the three crystal structures of **2** (R = Me) reported above. The results are shown in Figure 12, in the form of dispersion curves for the crystal orbitals (COs) arising from the eight radical singly occupied molecular orbitals (SOMOs) in the unit cell, as tracked along the reciprocal space direction that corresponds to the π-stacking direction of each cell.[36,37] In previous studies of the electronic structures of slipped π-stack bisdithiazolyls **1**, we concluded that their relatively low bandwidths (W = 0.4−0.5 eV) were associated with a loss in intermolecular overlap occasioned by the slippage of the radicals.[14,15] Calculations on a model π-stack consisting of

(35) Beer, L.; Brusso, J. L.; Haddon, R. C.; Itkis, M. E.; Oakley, R. T.; Reed, R. W.; Richardson, J. F.; Secco, R. A.; Yu, X. *Chem. Commun.* **2005**, 5745.

(36) In the two orthorhombic structures (*Cmca* and *Pccn*), there is an absolute correspondence between the directions of the real and reciprocal unit cell vectors, and in the 88 K ($P2_1/c$) structure the β angle is such that the correspondence is very nearly exact.

(37) The COs are plotted from Γ (0,0,0) to X ($^1/_2$,0,0) for the two orthorhombic structures, and from Γ (0,0,0) to Y (0,$^1/_2$,0) for the monoclinic cell. Note that, for the calculations on the 295 K structure, we used the special position of the primitive cell rather than that of the full *C*-centered version so as to allow for a more direct comparison of the three band structures.

perfectly superimposed radicals suggested that bandwidths approaching 2 eV could be achieved. At 295 K, in the *Cmca* structure, the alternating orientation of radicals along the π-stack produced by the *a*-glide precludes perfect superposition and reduces orbital interactions along the stack, that is, those associated with the S1−S4′ and S2−S2′ contacts. However, the same feature also allows for increased interactions between the stacks, that is, through the S1−S2′, S3−S3′, and S4−S4′ contacts, so that significant bandwidth can still be attained.

Based on the energetic spread of the eight COs, the estimated bandwidth *W* is close to 1.5 eV, approaching that predicted for a perfectly superimposed π-stacked structure.[38] On the basis of this description, such a bandwidth might well be expected to give rise to an $f = {}^1/_2$ metal.

The loss of *C*-centering occasioned by cooling crystals of **2** (R = Me) to 123 K, and the associated onset of an alternation in the plate-to-plate separation along the π-stack, should lead to the opening of an energy gap at the Fermi level and the creation of a semiconducting state. The band structure calculations on the *Pccn* cell support this conclusion, although the observed band gap E_g is only 0.09 eV. However, upon further cooling and transformation to the monoclinic $P2_1/c$ cell, the magnitude of the calculated band gap increases quite dramatically to 0.42 eV, in spite of the fact that the structural changes between the *Pccn* and $P2_1/c$ structures appear to be extremely small.

Discussion

The design of single-component conductive materials composed of neutral radicals requires the development of molecular building blocks which, in the solid state, give rise to a low on-site Coulomb repulsion *U* and a large bandwidth *W*. In principle, resonance-stabilized bisdithiazolyls **1** respond to both these challenges. Their delocalized spin distributions lead to reduced disproportionation energies and cell potentials relative to those seen in earlier generations of thiazyl radicals, while their exposed sulfur-rich peripheries should allow for strong intermolecular interactions. Moreover, the structural evidence to date indicates that these radicals resist carrier-quenching dimerization. However, the slipped π-stack packing motifs (Chart 1) that these systems invariably adopt[15,16] lead to a severe decrease in intrastack overlap and lowered bandwidths, as a result of which a metallic ground state has not been achieved.

Replacement of the pyridine ring of **1** with a pyrazine ring in **2** was therefore undertaken in the belief that removal of the R_2 group of **1** would favor more nearly superimposed π-stacking and lead to an improved bandwidth (Chart 1).[39] However, as the structures (Chart 2) of the two phases of **2** (R = Et) illustrated, removal of the steric protection afforded by the basal ligand also renders the radical vulnerable to cofacial σ-dimerization.[40] The α-dimer (R = Et) thus represents the first example of a heterocyclic thiazyl radical dimerized through a localized C−C σ-bond.[20] Moreover, its conversion to the β-isomer provides a sobering caveat that, in the absence of lattice effects, ring-opening S−S σ-dimerization of bisdithiazolyl radicals is the thermodynamically preferred outcome.

In the light of these results, the crystal structure of **2** (R = Me) at 295 K (*Cmca*), consisting of bisdithiazolyl radicals locked by glide planes into alternating but apparently evenly spaced π-stacked arrays, was a welcome and exciting finding. This is a hitherto unobserved packing pattern for a neutral radical ($f = {}^1/_2$) conductor, although similar symmetric ABABAB π-stacking arrangements defined by glide planes have been observed in CT salts.[41] The strongly interconnected π-stacks in **2** (R = Me) suggest a well-developed two-dimensional electronic structure, a view confirmed by the band structure calculations. Given the apparent convergence of the necessary energetic and structural features, it was at first surprising that its conductivity is activated, not metallic.

So why is **2** (R = Me) not a metal at room temperature? One possible reason is that the material is a Mott insulator.[41] The weak but increasing paramagnetism above 120 K could be interpreted in terms of evenly spaced (undimerized) π-stacks consisting of strongly antiferromagnetically coupled radicals. The activated conductivity would then be a consequence of strong electron correlation; that is, the bandwidth *W* is insufficient to overcome the Coulomb repulsion *U*. Although the band calculations indicate a remarkably high bandwidth ($W \approx 1.5$ eV) for a molecular material, even this may not be sufficient to offset short-range correlation.[42] The other possible explanation is that the material is a semiconductor. Indeed, such a description would be the natural default if the diamagnetic π-dimer stacked structure identified at 88 K were also observed at room temperature. The band gap value, $E_g = 0.42$ eV, estimated from the EHT calculations would then be satisfyingly close to the threshold optical excitation found from near-IR measurements. It would also be about twice the value of the thermal activation energy, $E_{act} = 0.19$ eV, obtained from the variable-temperature conductivity measurements, a result expected for an intrinsic semiconductor. The moderate response of the conductivity to pressure would also be in keeping with stacked π-dimer structures.[43] However, this simple explanation is, by itself, insufficient, as it ignores the magnetic and structural changes that occur upon heating the material above 120 K.

As noted earlier, previous work on diamagnetic π-stacked thiazyl dimers has shown that, with increasing temperature, an increase in the magnetic response is often observed.[33,34] This "spin breakout" can be rationalized in terms of a random uncoupling of dimers and the generation of radical defects. Figure 13 illustrates this process as it applies to the slightly tilted π-dimer stacks of the $P2_1/c$ structure of **2** (R = Me). In the absence of any residual defects (which are, in reality, present), the structure would be as shown in Figure 13A, with all radicals paired to afford a perfectly diamagnetic ground state. Heating the structure causes an opening of some of the dimers, to produce geminal (Figure 13B) and/or non-geminal (Figure

(38) In perfectly superimposed π-stacked CT salts of dithiadiazolyl and diselenadiazoyl radicals, EHT bandwidths approaching 3.0 eV have been reported. For example, see: Bryan, C. D.; Cordes, A. W.; George, N. A.; Haddon, R. C.; MacKinnon, C. D.; Oakley, R. T.; Palstra, T. T. M.; Perel, A. S. *Chem. Mater.* **1996**, *8*, 762.

(39) The removal of buffering R-groups to enhance intermolecular interactions was an approach used early on in the design of dithiadiazolyl radicals. For example, see: Cordes, A. W.; Haddon, R. C.; Hicks, R. G.; Kennepohl, D. K.; Oakley, R. T.; Schneemeyer, L. F.; Waszczak, J. V. *Inorg. Chem.* **1993**, *32*, 1554.

(40) This effect is well recognized for purely organic radicals. See, for example: Zaitsev, V.; Rosokha, S. V.; Head-Gordon, M.; Kochi, J. K. *J. Org. Chem.* **2006**, *71*, 520.

(41) Heuzé, K.; Fourmigué, M. A.; Batail, P.; Coulon, C.; Clérac, R. B.; Canadell, E. C.; Auban-Senzier, P. A.; Ravy, S. D.; Jérome, D. *Adv. Mater.* **2003**, *15*, 1251.

(42) Ohno, K.; Noguchi, N.; Yokoi, T.; Ishii, S.; Takeda, J.; Furuya, M. *ChemPhysChem* **2006**, *7*, 1820.

(43) Britten, J. F.; Clements, O. P.; Cordes, A. W.; Haddon, R. C.; Oakley, R. T.; Richardson, J. F. *Inorg. Chem.* **2001**, *40*, 6820.

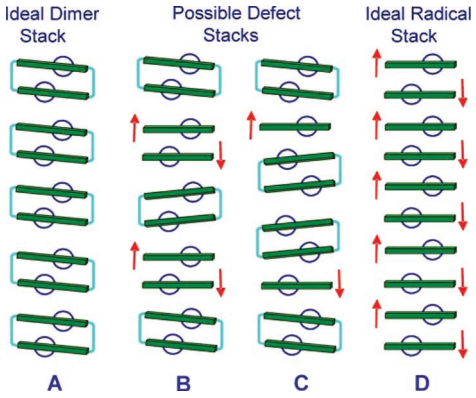

Figure 13. Radical defects (B, C) generated upon heating perfectly ordered π-dimer stacks (A). A fully symmetric π-radical stack (D) is also shown.

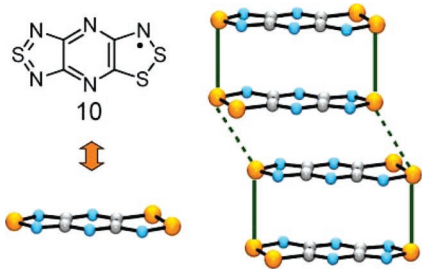

Figure 14. Head-over-tail π-dimer stacking in dithiazolyl radical **10**.

13C) radical defects. At the same time, the previously regular tilt angle (ϕ) of the dimers is replaced by a random clockwise or counterclockwise rocking. Any of these structural modifications, or a combination thereof, will give rise to a gradual increase in magnetization and, at the same time, lead to a loss of crystallographic correlation in the orientation of the molecules along the stacking direction. This loss of correlation creates the illusion of higher symmetry. The observation of C-centering and assignment of the *Cmca* space group is thus not a result of perfect ordering of uncoupled radicals, as depicted in Figure 13D, but rather a consequence of thermally induced disorder along the π-stacks of the $P2_1/c$ cell, with the *Pccn* cell representing an intermediate phase in this process. The elongated thermal ellipsoids for the sulfur atoms in the *Cmca* structure (Figure 2) attest to the fact that the high-symmetry space group is an artifact of the diffraction experiment and that, over the entire temperature range studied, the transport properties of the material are best rationalized in terms of a structure consisting of defect-contaminated π-dimer stacks.

Given the above structural description, we propose a hopping model[44] to account for the conductivity of **2** (R = Me) as a function of temperature. We have used this approach before to rationalize the transport properties of the dithiazolyl radical **10** (Figure 14),[34] the solid-state structure of which showed a head-over-tail π-dimer stacking motif similar to the ABABAB arrangement described here. In the present case, topological defects and lattice disorder give rise to a finite density of states (Figure 15) within the band gap of the ideal $P2_1/c$ structure (Figure 12), even at low temperatures (<120 K). With increasing temperature, the radical spins generated by uncoupling of the dimers increase the density of these defect states. These states are not localized and contribute to the conductivity. They may,

(44) Mott, N. F.; Davis, E. A. *Electronic Processes in Non-Crystalline Materials*, 2nd ed.; Oxford University Press: Oxford, 1993.

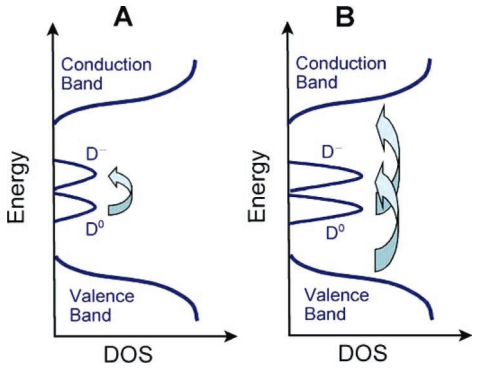

Figure 15. Schematic density of states (DOS) diagram showing donor (D^0) and acceptor (D^-) Hubbard defect bands in **2** (R = Me), with low-temperature excitations between these states (A) and high-temperature excitations from/to the valence/conduction bands (B).

however, be split by Coulomb correlations into donor (D^0) and acceptor (D^-) Hubbard sub-bands.[44] The low-temperature conductivity (<120 K) may thus be viewed as arising from variable-range hopping between these weakly metallic midgap states (Figure 15A). These processes can be collectively associated with a thermal activation energy E_{act} = 0.12 eV (Figure 9). At elevated temperatures (>120 K), the conductivity stems from hopping that also involves excitations between the midgap states and the band edges of either the valence or conduction bands (Figure 15B), processes for which E_{act} = 0.19 eV, a value in good agreement with the band gap estimated from the optical measurements and EHT calculations. The infrared spectrum can also be explained within this model. The poorly resolved background below 3000 cm^{-1} (Figure 11) can be ascribed to electronic excitations between the midgap states and the valence/conduction bands, while the strong, broad band above 3000 cm^{-1} corresponds to valence-to-conduction band excitations.

Summary and Conclusions. We have developed a synthetic route to a new class of resonance-stabilized radical, one based on the use of a pyrazine bridging unit between two 1,2,3-dithiazole rings. Two examples of these highly delocalized radicals **2** (R = Me, Et) have been characterized in solution by EPR spectroscopy and cyclic voltammetry. From these studies, we conclude that these materials should enjoy a relatively low onsite Coulomb repulsion *U* in the solid state. Structural studies on the ethyl derivative **2** (R = Et) reveal that the radicals crystallize in two different dimeric modifications; in both cases, the radical spins are paired and not available to serve as charge carriers.[20] By contrast, the corresponding methyl derivative **2** (R = Me) crystallizes in alternating ABABAB π-stacked arrays, with rows of π-stacks dovetailed together by π-type interannular S−S′ interactions. The conductivity of this material is the highest ever seen for a neutral thiazyl radical, with a room-temperature value $\sigma_{RT} \approx 0.001$ S cm^{-1}. The material is not, however, a metal, as the conductivity remains activated, even under an applied pressure of 5.5 GPa. The high-symmetry space group *Cmca* observed crystallographically at ambient temperatures is nonetheless consistent with an $f = {}^1/_2$ metallic state. Variable-temperature magnetic measurements confirm diamagnetic behavior below 120 K, and low-temperature crystallographic work establishes a sequential lowering in space group symmetry from *Cmca* (295 K) to *Pccn* (123 K) to $P2_1/c$ (88 K), changes which give rise to an opening of a band gap at the Fermi level and the formation of a semiconducting ground state. While the activated

conductivity at room temperature could be ascribed to Mott insulator behavior, we believe that the high-symmetry *Cmca* space group is an artifact arising from the loss of long-range correlation in the slightly tilted π-stacks of the $P2_1/c$ structure. As a result, at ambient temperatures, the material is still best described as a semiconductor, with conductivity arising from hopping within and to/from midgap states produced by radical defects present in the lattice. It remains to be seen if modifications to the framework of **2**, that is, changes in the R group or the replacement of sulfur by selenium, as has recently been achieved for **1**,[19] will afford more conductive materials, and perhaps a metallic ground state.

Experimental Section

General Procedures and Starting Materials. The reagents pyrazine, sodium azide, ammonium thiocyanate, tri-*n*-butylphosphine, thionyl chloride, pyridine, iron powder, gallium trichloride, Proton-Sponge, decamethylferrocene (DMFc), trimethyloxonium, and triethyloxonium tetrafluoroborates were obtained commercially. All were used as received, save for DMFc, which was sublimed and recrystallized from acetonitrile before use. All solvents were of at least reagent grade; acetonitrile (MeCN) and dichloroethane (DCE) were dried by distillation from P_2O_5. All reactions were performed under an atmosphere of dry nitrogen. 2,6-Dichloropyrazine **3**[45] and the corresponding diazide **4**[21] were prepared according to literature methods. Melting points are uncorrected. Fractional sublimations were performed in an ATS series 3210 three-zone tube furnace, mounted horizontally, and linked to a series 1400 temperature control system. Infrared spectra (Nujol mulls, KBr optics) were recorded on a Nicolet Avatar FTIR spectrometer (at 2 cm^{-1} resolution), and visible spectra were collected using a Beckman DU 640 spectrophotometer. ^1H and ^{31}P NMR spectra were run on a Bruker Avance 300 MHz NMR spectrometer. Low-resolution mass spectra (70 eV, EI, DEI and CI, DCI) were run on a Micromass Q-TOF Ultima Global LC/MS/MS system or a JEOL HX110 double-focusing mass spectrometer. Elemental analyses were performed by MHW Laboratories (Phoenix, AZ).

Preparation of 2,6-Diaminopyrazine, 5. Sodium azide (5.50 g, 84.6 mmol) was slowly added as a powdered solid to a stirred solution of dichloropyrazine **3** (6.00 g, 40.3 mmol) in 75 mL of dimethylsulfoxide, and the mixture was heated to 70 °C in an oil bath for 1 h. The turbid orange solution was poured onto 1 L of ice/water, and the resulting white fibrous precipitate of the diazide **4** was filtered off on a Büchner funnel and washed with water (*caution!*[46]). The crude (and still wet) diazide was transferred into a 500 mL flask, to which was added 200 mL of water, 100 mL of EtOH, 3 mL of HOAc, and iron filings (10.0 g). The mixture was heated to a gentle boil for 30 min, cooled, and filtered. The filtrate was made alkaline (to pH > 12) with NaOH, and the resulting gelatinous precipitate was filtered off. The aqueous filtrate was then flash evaporated and the residual solid extracted with 3 × 300 mL of boiling DCE. The combined extracts were evaporated to afford crude 2,6-diaminopyrazine **5** as an off-white solid. Recrystallization from DCE afforded fibrous needles; yield 3.10 g (28.2 mmol, 70% from **3**); mp 135−137 °C (lit.[21] mp 136−137 °C). IR: 3407 (w), 3312 (s), 3167 (s, br), 1632 (s), 1587 (m), 1537 (vs), 1293 (s), 1249 (m), 1137 (m), 1000 (m), 821 (m), 753 (w), 620 (w), 572 (w), 473 (w) cm^{-1}.

Preparation of 2,6-Diaminopyrazine-3,5-bisthiocyanate, 6. A solution of bromine (29.0 g, 0.181 mol) in 100 mL of cold MeOH was added dropwise to a cold (−78 °C) solution of NH_4SCN (27.6 g, 0.363 mol) in 500 mL of MeOH over 1 h to afford a colorless slurry. After 10 min, a solution of **5** (10.0 g, 0.0908 mol) in 100 mL of MeOH was added dropwise to the reaction mixture over 1 h, and the mixture was stirred for an additional hour at −78 °C. The mixture was warmed to room temperature and stirred for 16 h before being added to 2 L of ice/water. After 1 h, the yellow product **6** was filtered off and washed with water; yield 15.0 g (0.0669 mol, 74%). IR: 3442 (w), 3339 (w), 3183 (w), 2168 (s), 2157 (s), 1626 (s), 1513 (s), 1430 (m), 1309 (m), 1254 (m), 1151 (w), 1036 (w), 764 (s), 676 (m), 480 (s), 454 (m), 409 (w) cm^{-1}. Anal. Calcd for $C_6H_4N_6S_2$: C, 32.13; H, 1.80; N, 37.47. Found: C, 32.17; H, 1.59; N, 37.20.

Preparation of 2-Tributylphosphinimino-6-aminopyrazine-3,5-dithiol, 8. Tributylphosphine (27.0 mL, 0.108 mol) was added to a thick slurry of **6** (10.4 g, 0.0463 mol) in 250 mL of MeCN to give a red solution. Upon brief stirring, a fine orange precipitate was formed. After 30 min, water (1.70 mL, 0.0943 mol) was added, and the reaction mixture was stirred for an additional 30 min before filtration to afford an orange microcrystalline powder. The product, **8**, which crystallizes as a hydrate, was washed with 2 × 150 mL of MeCN and 1 × 150 mL of diethyl ether; yield 12.8 g (0.0326 mol, 70%); mp 115 °C dec. IR: 3422 (w), 3276 (w), 3084 (w), 2252 (w), 1582 (m), 1553 (m), 1521 (m), 1421 (m), 1358 (m), 1292 (m), 1225 (m), 1209 (m), 1144 (m), 1113 (w), 1096 (w), 1044 (m), 937 (m), 906 (m), 891 (w), 833 (w), 780 (w), 459 (w) cm^{-1}. ^{31}P NMR (δ, $CDCl_3$): 54.6 (s, 1P). Anal. Calcd for $C_{16}H_{33}N_4OPS_2$: C, 48.95; H, 8.47; N, 14.27. Found: C, 48.22; H, 7.93; N, 13.91. The crude material was desolvated by heating it at 80 °C/10^{-3} Torr.

Preparation of 4*H*-Bis[1,2,3]dithiazolo[4,5-b:5′,4′-e]pyrazin-2-ium Tetrachlorogallate, [2][$GaCl_4$] (R = H). Pyridine (6.40 mL, 0.0791 mol) was added to a slurry of **8** (14.9 g, 0.0398 mol) in 400 mL of MeCN. A solution of $SOCl_2$ (31.0 mL, 0.425 mol) in 30 mL of MeCN was added dropwise to the slurry over 30 min to give a brown mixture (slight exotherm), which was set to reflux for 1 h. After the mixture cooled to room temperature, the brown solid [**2**][Cl] (R = H) was filtered off and washed with 200 mL of MeCN and 200 mL of DCE; yield 9.92 g (0.0369 mol, 93%). IR: 1634 (w), 1562 (w), 1548 (w), 1535 (w), 1425 (s), 1319 (s), 1083 (m), 885 (w), 868 (w), 802 (w), 751 (w), 718 (m), 683 (w), 618 (m), 506 (m), 481 (m), 447 (m) cm^{-1}. Gallium trichloride (8.00 g, 0.0454 mol) was added to a slurry of crude [**2**][Cl] (R = H) (10.1 g, 0.0375 mol) in 150 mL of MeCN to afford a dark violet-blue solution, which was stirred for 15 min before being filtered to remove any undissolved material. The solvent was removed from the filtrate by flash distillation to leave a purple-bronze residue that was triturated in 30 mL of a 1:1 HOAc/DCE solution. The gallate [**2**][$GaCl_4$] (R = H) was filtered and washed several times with HOAc/DCE mixtures and then neat HOAc, followed by diethyl ether; yield 10.3 g (0.0231 mol, 62%). IR: 3194 (w), 1615 (w), 1559 (w), 1544 (w), 1427 (m), 1415 (m), 1330 (m), 1311 (m), 1088 (w), 880 (w), 847 (w), 723 (m), 635 (m), 505 (s), 479 (s) cm^{-1}.

Preparation of Bis[1,2,3]dithiazolo[4,5-b:5′,4′-e]pyrazine, 9. A sample of [**2**][$GaCl_4$] (R = H) (8.19 g, 0.0184 mol) was dissolved in 150 mL of MeCN to afford a blue solution that was filtered to remove any undissolved solid. A solution of Proton-Sponge (4.76 g, 0.0222 mol) in 150 mL of MeCN was added dropwise to the filtrate over 15 min. After 20 min, the blue-gray solid **9** was collected by filtration and washed with 3 × 100 mL of MeCN; yield 4.30 g (0.0180 mol, 100%). IR: 1605 (w), 1412 (s), 1264 (s), 1124 (w), 1086 (m) cm^{-1}.

Preparation of 4-Methyl-4*H*-bis[1,2,3]dithiazolo[4,5-b:5′,4′-e]-pyrazin-2-ium Tetrafluoroborate, [2][BF_4] (R = Me). Proton-Sponge (2.03 g, 0.00945 mol) was added to a slurry of Me_3OBF_4 (5.58 g, 0.0377 mol) in 50 mL of DCE to afford a yellow slurry. Zwitterion **9** (4.39 g, 0.0189 mol) was then added, and the blue-green reaction mixture was stirred for 16 h at room temperature. The brown solid was filtered off and washed with 2 × 40 mL of DCE. In order to remove protonated impurities, the crude product was rapidly stirred in 200 mL of warm (70 °C) HOAc for 40 min. The material so obtained was further purified by double recrystallization from MeCN to afford [**2**][BF_4] (R = Me)

(45) (a) Klein, B.; Hetman, N. E.; O'Donnell, M. E. *J. Org. Chem.* **1963**, *28*, 1682. (b) Klein, B.; Berkowitz, J. *J. Am. Chem. Soc.* **1959**, *81*, 5160.
(46) Azides can be explosive, although there is no evidence that this one is. Avoid spatulas and glass frits, and minimize exposure to light (the dry solid turns blue on exposure to air).

as lustrous red crystals; yield 1.64 g (0.00491 mol, 26%); mp 273 °C dec. IR: 1614 (w), 1541 (m), 1503 (s), 1337 (s), 1198 (m), 1120 (m), 1085 (s), 1051 (s), 1019 (s), 951 (w), 891 (m), 877 (w), 720 (m), 663 (s), 526 (m), 513 (w), 488 (m), 477 (m) cm^{-1}. ^1H NMR (δ, CD_3CN): 3.49 (s, 3H, CH_3). UV−vis (MeCN): λ_{max} 623 nm (log ϵ = 4.6). Anal. Calcd for $C_5H_3BF_4N_4S_4$: C, 17.97; H, 0.90; N, 16.77. Found: C, 18.08; H, 0.73; N, 17.00.

Preparation of 4-Ethyl-4*H*-bis[1,2,3]dithiazolo[4,5-b:5′,4′-e]-pyrazin-2-ium Tetrafluoroborate, [2][BF$_4$] (R = Et). Proton-Sponge (1.76 g, 0.00819 mol) was added to a colorless solution of Et_3OBF_4 (6.18 g, 0.0325mol) in 60 mL of DCE to give a clear yellow solution. Zwitterion **9** (3.77 g, 0.0162 mol) was then added, and the blue-green reaction mixture was stirred for 16 h at room temperature. The red-brown crude product was collected by filtration and washed with 2 × 45 mL of DCE. To remove protonated impurities, the crude product was warmed at 70 °C in 200 mL of HOAc for 40 min. This material was further purified by double recrystallization from MeCN to give [**2**][BF_4] (R = Et) as lustrous red crystals; yield 2.70 g (0.00775 mol, 48%); mp 276 °C dec. IR: 1538 (m), 1503 (s), 1335 (s), 1198 (m), 1181 (m), 1069 (s), 1032 (s), 887 (m), 789 (m), 722 (m), 657 (m), 549 (w), 519 (m), 512 (m), 483 (m) cm^{-1}. ^1H NMR (δ, CD_3CN): 4.02 (q, 2H, NCH_2CH$_3$, J = 7.2 Hz), 1.27 (t, 3H, NCH$_2$$CH_3$, J = 7.2 Hz). UV−vis (MeCN): λ_{max} 623 nm (log ϵ = 4.5). Anal. Calcd for $C_6H_5BF_4N_4S_4$: C, 20.70; H, 1.45; N, 16.09. Found: C, 20.86; H, 1.25; N, 16.31.

Preparation of 4-Methyl-4*H*-bis[1,2,3]dithiazolo[4,5-b:5′,4′-e]-pyrazin-3-yl, 2 (R = Me). A carefully degassed (four freeze−pump−thaw cycles) solution of [**2**][BF_4] (R = Me) (0.250 g, 0.748 mmol) in 75 mL of MeCN was added to an equally degassed solution of DMFc (0.256 g, 0.784 mmol) in 130 mL of MeCN. After 30 min, fine gold crystals of analytically pure **2** (R = Me) were collected by filtration and washed with 3 × 15 mL of MeCN; yield 0.152 g (0.614 mmol, 84%). IR: 1308 (w), 1212 (w), 1030 (m), 842 (w), 697 (w), 650 (w), 516 (m), 483 (w), 433 (w) cm^{-1}. Crystals suitable for crystallographic work and single-crystal conductivity measurements were obtained by the slow diffusion of a degassed solution of [**2**][BF_4] (R = Me) (0.030 g, 0.0898 mmol) in 10 mL of MeCN into a similarly degassed solution of DMFc (0.030 g, 0.0919 mmol) in 15 mL of MeCN through a fine-porosity frit. The fine copper needles were harvested after 16 h. Anal. Calcd for $C_5H_3N_4S_4$: C, 24.28; H, 1.22; N, 22.65. Found: C, 24.40; H, 1.20; N, 22.81.

Preparation of 4-Ethyl-4*H*-bis[1,2,3]dithiazolo[4,5-b:5′,4′-e]-pyrazin-3-yl, 2 (R = Et). A sample of [**2**][BF_4] (R = Et) (0.700 g, 0.00201 mol) and DMFc (0.689 g, 0.00211 mol) were combined in 30 mL of degassed MeCN to give a fuschia-colored solution. After 2 h, the light brown solid was filtered off and washed with 3 × 10 mL of MeCN; yield 0.393 g (0.00150 mol, 75%). Vacuum sublimation of the isolated material at 10^{-4} Torr in a three-zone furnace along a temperature gradient from 100 °C to 50 °C gave a mixture of amber blocks of α-[**2**]$_2$ and black needles of β-[**2**]$_2$, which could be manually separated. Resublimation of the mixed material at 10^{-4} Torr along a temperature gradient from 110 °C to 50 °C afforded 100% black needles of β-[**2**]$_2$. IR of α-[**2**]$_2$: 1606 (w), 1582 (w), 1562 (m), 1526 (w), 1496 (w), 1343 (w), 1262 (w), 1227 (w), 1179 (w), 1123 (w), 1067 (w), 1002 (w), 864 (w), 836 (w), 796 (w), 774 (w), 694 (m), 662 (w), 641 (m), 550 (w), 511 (w), 483 (w), 467 (w), 429 (w) cm^{-1}. IR of β-[**2**]$_2$: 1534 (m), 1434 (s), 1403 (w), 1353 (w), 1334 (s), 1262 (m), 1224 (s), 1183 (m), 1065 (m), 880 (s), 788 (w), 727 (m), 668 (w), 648 (w), 648 (w), 546 (w), 485 (w), 464 (w), 420 (w) cm^{-1}. Anal. Calcd for β-phase $C_6H_5N_4S_4$: C, 27.57; H, 1.93; N, 21.43. Found: C, 27.61; H, 2.00; N, 21.26.

Cyclic Voltammetry. Cyclic voltammetry was performed using a PINE Bipotentiostat, model AFCClBP1, with scan rates of 50−100 mV s^{-1} on solutions (<10^{-3} M) of [**2**][BF_4] (R = Me, Et) in oxygen-free MeCN (dried by distillation from CaH_2) containing 0.1 M tetra-*n*-butylammonium hexafluorophosphate. Potentials were scanned with respect to the quasi-reference electrode in a single-compartment cell fitted with Pt electrodes and referenced to the Fc/Fc$^+$ couple of ferrocene at 0.38 V vs SCE.[47] The $E_{pa}-E_{pc}$ separation of the reversible couple was within 10% of that of the Fc/Fc$^+$ couple.

EPR Spectra. The X-band EPR spectra were recorded at ambient temperature using a Bruker EMX-200 spectrometer on samples of **2** (R = Me, Et) dissolved in degassed dichloromethane. Hyperfine coupling constants were obtained by spectral simulation using Simfonia.[48]

X-ray Measurements. The needle of **2** (R = Me) used for the 295 and 123 K data sets was glued to a glass fiber with epoxy, and the crystal for the 88 K data set was mounted on a loop with paratone. The 295 and 123 K data sets were collected using ω-scans with a Bruker SMART6000 CCD detector on a D8 three-circle goniometer and parallel-focused Cu Kα radiation from a Rigaku RU-200 fine-focus rotating anode generator at 5 kW. The 88 K data set was collected using ϕ- and ω-scans on a Bruker SMART APEX II diffractometer with an APEX II CCD area detector on a D8 three-circle goniometer and Mo Kα (λ = 0.71073 Å) radiation. The data were scanned using Bruker's APEX 2 program and integrated using Bruker's SAINT software.[49] Processing of all the data was completed using the APEX 2 software by direct methods using SHELXS-90[50] and refined by least-squares methods on F^2 using SHELXL-97,[51] incorporated in the SHELXTL[52] suite of programs. A merohedral twin law (180° rotation about the *c*-axis) was applied in order to refine the 88 K data. All non-hydrogen atoms were refined anisotropically; hydrogen atoms were located on difference maps and refined isotropically. Details of data collection and refinement are presented in Table 2.

Band Structure Calculations. Band electronic structure calculations were performed with the EHMACC suite of programs[53] using the Coulomb parameters of Baasch, Viste, and Gray[54] and a quasi-split-valence basis set adapted from Clementi and Roetti;[55] numerical values are tabulated elsewhere.[56] The off-diagonal elements of the Hamiltonian matrix were calculated with the standard weighting formula.[57] Atomic positions were taken from the crystallographic data.

Magnetic Susceptibility Measurements. Magnetic susceptibility measurements on **2** (R = Me) were performed over the temperature range 9−310 K on a George Associates Faraday balance operating at 0.5 T.

Ambient-Pressure Conductivity Measurements. Ambient-pressure single-crystal conductivity measurements on **2** (R = Me) were made using a four-probe configuration along the needle axis (which corresponds to the crystallographic *x*-direction), with in-line contacts made using silver paint. The measurements were performed on a custom-made helium variable-temperature probe using a Lake Shore 340 temperature controller. A Keithley 236 unit was used as a voltage source and current meter, and two 6517A Keithley electrometers were used to assess the voltage drop between the potential leads in the four-probe configuration.

High-Pressure Conductivity Measurements. High-pressure temperature conductivity experiments on **2** (R = Me) were carried out in

(47) Boeré, R. T.; Moock, K. H.; Parvez, M. *Z. Anorg. Allg. Chem.* **1994**, *620*, 1589.
(48) *WinEPR Simfonia*, version 1.25; Bruker Instruments, Inc.: Billerica, MA, 1996.
(49) *SAINT*, version 6.22; Bruker Advanced X-ray Solutions, Inc.: Madison, WI, 2001.
(50) Sheldrick, G. M. SHELXS-90. *Acta Crystallogr. A* **1990**, *46*, 467.
(51) Sheldrick, G. M. *SHELXL-97*, Program for the Refinement of Crystal Structures; University of Göttingen: Göttingen, Germany, 1997.
(52) *SHELXTL*, Version 6.12, Program Library for Structure Solution and Molecular Graphics; Bruker Advanced X-ray Solutions, Inc.: Madison, WI, 2001.
(53) EHMACC, Quantum Chemistry Program Exchange, program no. 571.
(54) Baasch, H.; Viste, A.; Gray, H. B. *Theor. Chim. Acta* **1965**, *3*, 458.
(55) Clementi, E.; Roetti, C. *At. Data Nucl. Data Tables* **1974**, *14*, 177.
(56) Cordes, A. W.; Haddon, R. C.; Oakley, R. T.; Schneemeyer, L. F.; Waszczak, J. V.; Young, K. M.; Zimmerman, N. M. *J. Am. Chem. Soc.* **1991**, *113*, 582.
(57) Ammeter, J. H.; Bürgi, H. B.; Thibeault, J. C.; Hoffmann, R. *J. Am. Chem. Soc.* **1978**, *100*, 3686.

a cubic anvil press[58] using pyrophyllite ($Al_4Si_8O_{20}(OH)_4$) as the pressure transmitting medium. Sample pressure was determined from previous calibrations of the applied hydraulic load against pressures of structure transformations in standards at room temperature (Hg L ↔ I at 0.75 GPa, Bi I ↔ II at 2.46 GPa, Tl 1 ↔ III at 3.70 GPa, and Ba 1 ↔ II at 5.5 GPa).[59] Temperature was applied by Joulean heating of a cylindrical Nb foil (0.127 mm thick) furnace and monitored with a Pt/(Pt + 10% Rh) thermocouple, using a pressure-corrected electromotive force.[59,60] Two Pt electrodes contacted the disk-shaped (∼6.1 mm diameter and ∼0.35 mm thick), pre-compacted powder sample which was contained in a boron nitride ($\sigma_{BN} \approx 10^{-11}$ S cm^{-1}) cup. Four-wire alternating current (Solartron 1260 impedance analyzer) resistance measurements were made at a frequency of 1 kHz. Separate experiments were performed at room temperature vs pressure (0.3−5.5 GPa) and at fixed pressures vs temperature (22−90 °C). In the constant room-temperature experiments, resistance was measured on increasing/decreasing pressure over 5−6 h. In the variable-temperature experiments, resistance was measured at fixed temperature intervals of 5−8 °C on heating/cooling at constant pressure. Pressure was increased and the temperature was cycled again. The contiguous disk-shaped sample was extracted from the recovered pressure cell, and the sample geometry was measured to convert resistance to conductivity. The IR spectrum of the recovered sample showed no change upon comparison with the pre-compression spectrum.

(58) Secco, R. A. *Can. J. Phys*. **1995**, *73*, 287.
(59) Secco, R. A.; Schloessin, H. H. *J. Appl. Phys*. **1986**, *60*, 1625.
(60) Bundy, F. P. *J. Appl. Phys*. **1961**, *32*, 483.

Acknowledgment. We thank the Natural Sciences and Engineering Research Council of Canada (NSERCC) for financial support. We also acknowledge the NSERCC for a Canada Graduate Scholarship to A.A.L. and the Canada Council for a Killam Research Fellowship to R.T.O. We are grateful to Dr. Mikhail Itkis and Prof. Robert Haddon of the University of California at Riverside for performing single-crystal conductivity, near-IR, and magnetic measurements on **2** (R = Me).

Supporting Information Available: Complete ref 33b, packing diagrams, and intermolecular contacts (PDF); details of X-ray crystallographic data collection and structure refinement, tables of atomic coordinates, bond distances and angles, anisotropic thermal parameters, and hydrogen atom positions (CIF). This information is available free of charge via the Internet at http://pubs.acs.org.

JA071218P